Ultrahigh-contrast and large-bandwidth thermal rectification in near-field electromagnetic thermal transfer between nanoparticles

Linxiao Zhu and Clayton R. Otey

Department of Applied Physics, Stanford University, Stanford, California 94305, USA

Shanhui Fan[*]

Department of Electrical Engineering, Ginzton Laboratory, Stanford University, Stanford, California 94305, USA

We exploit the unique properties of optical waves in nanophotonic structures to enhance the capabilities for active control of electromagnetic thermal transfer at nanoscale. We show that the near-field thermal transfer between two nanospheres can exhibit a thermal rectification effect with very high contrast and large operating bandwidth. In this system, the scale invariance properties of the resonance modes result in a large difference in the coupling constants between relevant modes in the forward and reverse scenarios. Such a difference provides a mechanism for thermal rectification. The two-sphere system can also exhibit negative differential thermal conductance.

I. INTRODUCTION

Active control of thermal transfer in nanoscale represents an exciting new frontier in thermal and nanosciences. In recent years, significant progress has been made to realize novel active thermal devices, such as thermal diodes,[1–5] transistors,[6] and switches,[7,8] exploiting new capabilities for controlling the properties of phonon and electron transport in nanoscale. Since photons are also major heat carriers, there is also significant emerging interest towards active control of nanoscale electromagnetic heat transfer, exploiting the unique properties of optical waves in nanophotonic structures.[9–21]

In this paper, we consider near-field thermal transfer between two nanospheres. Since these spheres are much smaller than the free-space wavelength for the relevant resonance modes, it is known that their resonances are scale invariant, i.e., the resonance frequencies are independent of the radius of the sphere, whereas the spatial distribution of the resonance modal field scales directly with the radius of the sphere.[22] Here, we show that such a scale invariance property results in a significant asymmetry in the relevant coupling constants between the modes in the spheres, and hence provides a rectification mechanism that is distinctly different from all previous works. For a photon-based thermal rectifier, such a mechanism significantly enhances its performance. We also show that the three-dimensional nanoscale modal confinement in these systems directly enables high-speed operation of the device.

II. BRIEF REVIEW OF PHOTON-BASED THERMAL RECTIFIERS

A thermal rectifier, or thermal diode, is a two-body device that operates in a nonequilibrium condition such that for a given temperature bias, the magnitude of heat flow between the bodies depends on the direction of the temperature bias. The performance of a thermal rectifier can be characterized by the rectification contrast ratio, defined as

$$R = \frac{Q_f - Q_r}{Q_r}, \tag{1}$$

where Q_f and Q_r are the net heat transfer in the forward and reverse bias cases, respectively.

All previous works on photon-based near-field thermal rectifier[9–13] utilize the parallel-plate geometry [see Fig. 1(a)] and are based on the mechanism shown in Figs. 1(b)–1(d). In this mechanism, one considers two bodies, each supporting a resonance with a temperature-dependent resonance frequency. At the same temperature, the resonance frequencies of the two bodies are different [see Fig. 1(b)]. Thermal rectification is then accomplished when the two bodies are at different temperatures, such that in the forward bias scenario there is an overlap of the resonance frequencies between the two bodies, and hence significant thermal transfer occurs [see Fig. 1(c)], whereas in the reverse bias scenario, there is no overlap in the resonance frequencies and hence thermal transfer is suppressed [see Fig. 1(d)]. This mechanism, which has been the basis for near-field photon-based thermal rectification for several material systems,[9–13] is also closely related to the mechanism to achieve phonon-based thermal diode through matching and/or mismatching of the energy spectra across the interface.[1,3]

In the actual simulation results, however, Refs. 9–13 provide only limited contrast between the forward and the reverse bias directions. In the parallel-plate geometry [see Fig. 1(a)], there exist significant nonresonant components for the heat transfer, which remains the same in both forward and the reverse bias scenarios, and hence limits the contrast ratio for the rectification scheme.[11] While efforts have been made in Refs. 12 and 13, to improve the contrast ratio in parallel-plate geometry, the improvement is observed either with the plate-plate separation at a single nanometer scale, or with material systems that provide almost no near-field enhancement of thermal transfer.

III. THERMAL RECTIFICATION BETWEEN TWO NANOSPHERES

In this section, we show that there exists a much stronger rectification effect in thermal transfer between nanospheres consisting of the same type of SiC [see Fig. 1(e)].
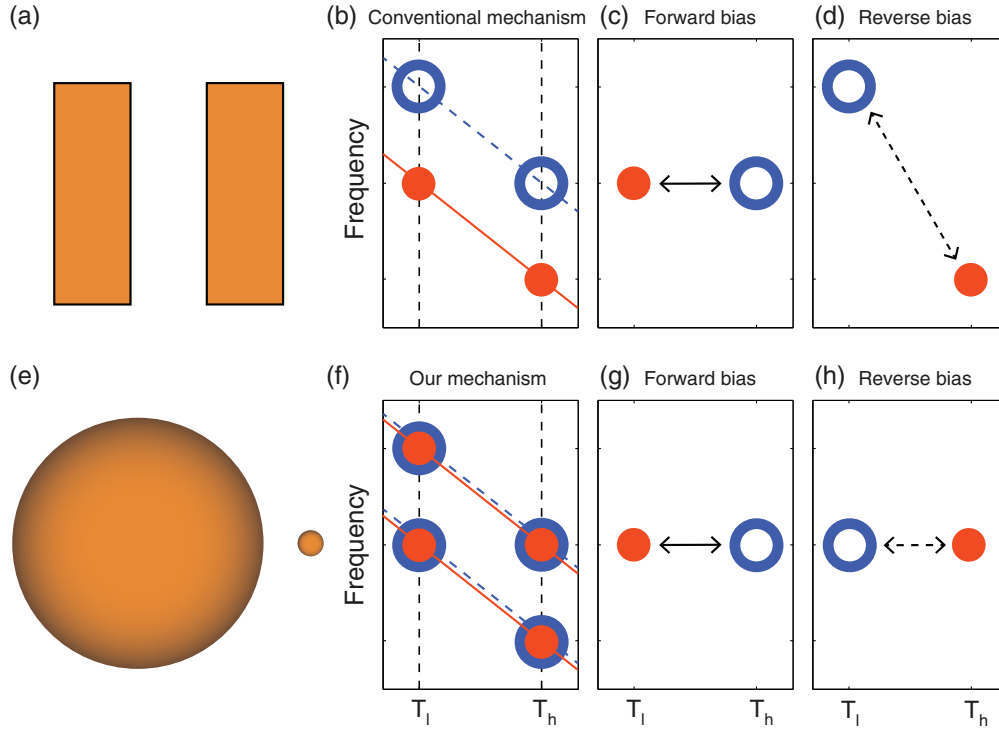
FIG. 1. (Color online) (a) Conventional device geometry for thermal rectification between two bodies consisting of two parallel plates. (b) The red solid and blue dashed lines denote the temperature dependence of a resonance of each body, respectively. The vertical dashed lines mark the operating temperatures T_h and T_l. The red circles and the blue rings mark the resonance frequencies of two bodies at the operating temperatures, respectively. (c) The (overlapping) resonance frequencies of two bodies in the forward bias scenario in the conventional mechanism. (d) The (nonoverlapping) resonance frequencies of two bodies in the reverse bias scenario in the conventional mechanism. (e) Our device geometry for thermal rectification. For our representative implementation in our paper, two spheres have the radii of 96 and 10 nm, respectively, and the sphere-sphere distance is 26 nm. (f)–(g) Illustration of our mechanism for thermal rectification. The symbols have the same meaning as (b)–(d). Notice that the two bodies are on resonance in both the forward and reverse bias scenarios.

A. Material properties and modal structures of SiC nanospheres

We start by briefly reviewing aspects of the electromagnetic modal structure of the SiC nanospheres that are relevant for the understanding of the rectification effect. As a representative implementation, the larger sphere has a radius of 96 nm and is maintained at a temperature T_h (or T_l). The smaller sphere has a radius of 10 nm and is maintained at a temperature T_l (or T_h). The two spheres are separated by a 26-nm vacuum gap. Both of the spheres are made of the same polytype 3C-SiC.[23,24] In the simulation below, we will make use of the temperature-dependent dielectric function of 3C-SiC (see Ref. 24), which is given by the expression

$$\epsilon(\omega) = \epsilon_\infty \frac{\omega_{\mathrm{LO}}^2 - \omega^2 - i\gamma\omega}{\omega_{\mathrm{TO}}^2 - \omega^2 - i\gamma\omega}, \tag{2}$$

where

$$
\begin{aligned}
\epsilon_\infty &= 6.7 \exp[5 \times 10^{-5}(T - 300)], \\
\omega_{\mathrm{LO}} &= 182.7 \times 10^{12} - 5.463 \times 10^9 (T - 300) \ \mathrm{rad\,s}^{-1}, \\
\omega_{\mathrm{TO}} &= 149.5 \times 10^{12} - 4.106 \times 10^9 (T - 300) \ \mathrm{rad\,s}^{-1}, \\
\gamma &= 6.6 \times 10^{11} \left[1 + \frac{2}{\exp\left(\frac{\hbar\omega_{\mathrm{TO}}}{2k_B T}\right) - 1} \right] \mathrm{rad\,s}^{-1},
\end{aligned}
\tag{3}
$$

with T in units of Kelvin. As the temperature increases, the resonance frequencies of the phonon-polariton shift and their linewidth increase.[24] All these effects are included in our theory and simulations.

We use the bulk dielectric function of 3C-SiC in the nanoparticle calculation. In previous studies, it is known that the phonon frequencies of 3C-SiC nanoparticles,[25,26] and the linewidth of various nanocrystals[27,28] typically have values that deviate from that of the bulk. However, in most cases, these size effects are significant only for particles with sizes smaller than 10 nm.[29] Also, while in this paper we use SiC, other polar or plasmonic materials that support narrow-banded near-field heat transfer can also be used to construct the device.

We define the direction connecting the centers of the two spheres as the z direction. Since the two-sphere geometry has a rotational symmetry around the z axis, the z-component m of the angular momentum is conserved.[30] Therefore the total heat transfer can be separated into different channels, with different m values.

The thermal transfer is dominated by the lowest few m channels,[30] and as an illustrative example, we present the properties of the resonant modes that are involved in the thermal transfer in the $m = 0$ channel. With $m = 0$, different modes of the individual spheres can be labeled with different total angular momentum L. For the large sphere with a radius of 96 nm, we plot in Fig. 2(a) the resonance frequencies of modes
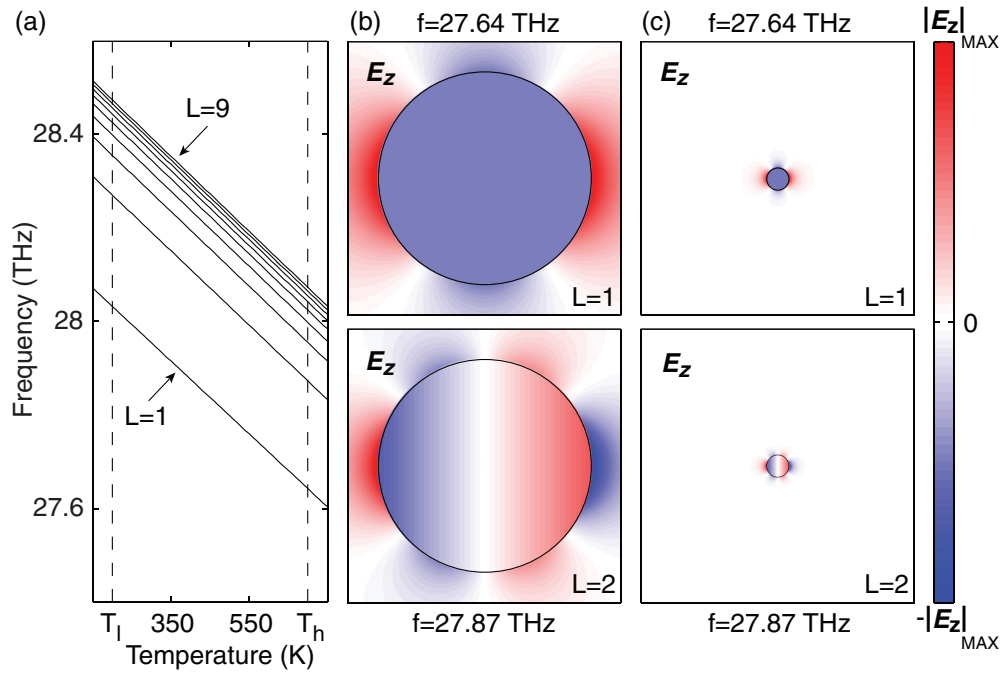
FIG. 2. (Color online) (a) The solid black lines denote the temperature dependence of resonance frequencies of $m = 0$ modes with different L for a deep-subwavelength 3C-SiC sphere. At a given temperature, the resonance frequencies increase with L. We show here modes from $L = 1$ to 9. The vertical dashed lines mark the operating temperatures T_h and T_l. (b)–(c) The electric field E_z distribution of $L = 1$ and 2 modes, with $m = 0$, in x-z plane with $y = 0$. The z axis is the horizontal direction. The radii of the spheres are 96 nm in (b) and 10 nm in (c).

with different L as a function of temperature. The resonance frequencies here are determined in full-field simulations using the temperature-dependent dielectric function of 3C-SiC.[23,24] The frequencies of ω_L of the Lth mode are described very well with[22]

$$\mathrm{Re}(\epsilon(\omega_L)) = -\frac{L + 1}{L}, \qquad (4)$$

where ϵ is the temperature-dependent dielectric function of the 3C-SiC.

In Fig. 2(b), we plot the spatial field distribution of the E_z fields for the $L = 1$ and $L = 2$ modes when the large sphere has maintained a temperature of 700 K. The $L = 1$ mode, which has a frequency of 27.64 THz, has a uniform E_z field within the sphere. The $L = 2$ mode, which has a frequency of 27.87 THz, has a nodal plane within the sphere in its E_z field distributions.

Since the sizes of both spheres are considerably smaller than the relevant free space wavelength of about 10.8 μm for the modes here, we are in the quasistatic regime. As a result, the resonance frequency of the sphere is in fact independent of the radius of the spheres. This can also be seen by noting that Eq. (4) has no dependency on the radius of the spheres. Thus, for the small sphere with a radius of 10 nm, the temperature dependence of the resonance frequencies of its various modes are also depicted by the *same* plot of Fig. 2(a) as for the large sphere. In Fig. 2(c), we plot the spatial field distribution of E_z fields for the $L = 1$ and 2 modes for the small sphere. We see that the modal field distribution for the small sphere is an exact scaled version of the fields for the large sphere, due to the scale-invariant properties of the modal fields in the quasistatic limit.[22]

When two spheres are brought in close proximity to each other, the total angular momentum L is no longer conserved. Thus, within each m channel, a mode in one of the spheres with a given L can couple to all other modes in the other sphere with different values of L. The dominant contributions to the thermal transfer, however, occur between modes that have similar resonance frequencies.

B. Mechanism for thermal rectification in two-sphere system

We now demonstrate that strong rectification can be accomplished in the two-sphere system, based on the modal properties as discussed above. As an illustration, we choose $T_h = 700$ K and $T_l = 200$ K, corresponding to the two dashed lines in Fig. 2(a).

In the forward bias scenario, where the large sphere is maintained at $T_h = 700$ K and the small sphere is maintained at $T_l = 200$ K, we see from Fig. 2(a) that the higher-order modes of the large sphere, including the $L = 2$ mode, are in resonance with the $L = 1$ mode of the small sphere. The couplings between these modes provide the dominant contributions to the heat transfer. As an illustration, we plot together the $L = 2$ mode of the large sphere, and $L = 1$ mode of the small sphere in Fig. 3(a). For the rest of the paper, we denote the Lth modes for the two spheres as $|L\rangle_{\mathrm{large}}$ and $|L\rangle_{\mathrm{small}}$, respectively. We represent the coupling constant between these two modes as $_{\mathrm{small}}\langle 1 | \mathbf{O} | 2\rangle_{\mathrm{large}}$, where $\mathbf{O}$ represents the coupling operator.

In contrast, in the reverse bias scenario, where the large sphere is at $T_l = 200$ K, and the small sphere is at $T_h = 700$ K, the dominant contributions to the heat transfer come from the
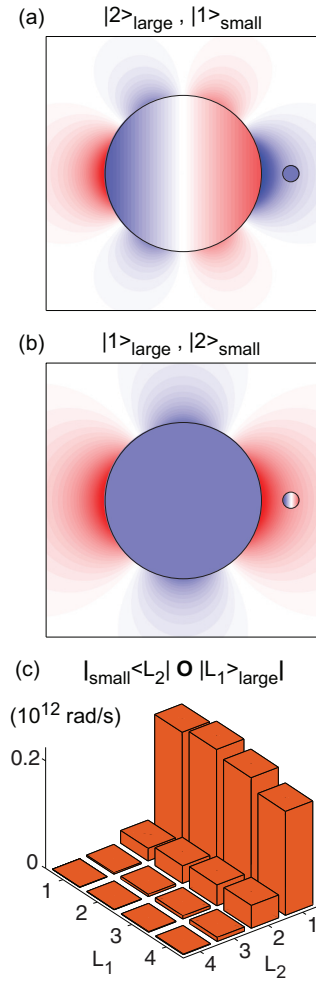
(a) $|2\rangle_{\text{large}}$, $|1\rangle_{\text{small}}$

(b) $|1\rangle_{\text{large}}$, $|2\rangle_{\text{small}}$

(c) $|_{\text{small}}\langle L_2|\,\mathbf{O}\,|L_1\rangle_{\text{large}}|$

$(10^{12}$ rad/s$)$

FIG. 3. (Color online) (a) The field distribution E_z of $|2\rangle_{\text{large}}$ and $|1\rangle_{\text{small}}$. (b) The field distribution (E_z) of $|1\rangle_{\text{large}}$ and $|2\rangle_{\text{small}}$. In (a) and (b), for the mode of the small sphere, we only show the field inside the small sphere. (c) Coupling constants between the four lowest order modes of the two spheres in the $m = 0$ channel. L_1 and L_2 are the total angular momenta of the modes of the large and the small spheres, respectively. (a)–(c) use the same parameters of the representative device implementation [Fig. 1(e)].

$L = 1$ mode $|1\rangle_{\text{large}}$ of the large sphere and modes with higher L of the small sphere. Again, as an illustration, we plot together the $L = 1$ mode $|1\rangle_{\text{large}}$ of the large sphere, and $L = 2$ mode $|2\rangle_{\text{small}}$ of the small sphere in Fig. 3(b). The coupling constant between these two modes is $_{\text{small}}\langle 2|\,\mathbf{O}\,|1\rangle_{\text{large}}$.

In this system, in both the forward and the reverse bias scenario, there always exist modes in the two spheres that are on-resonance with each other [see Figs. 1(g)–1(h)]. This is in contrast with the rectifier considered in Refs. 9–13, where in the reverse bias scenario the resonances of the two bodies were off-resonance from each other [see Figs. 1(c) and 1(d)]. In this system, the rectification arises from the very large difference in coupling constants between the modes that are relevant in the different bias scenarios, i.e., the large contrast in magnitude between $_{\text{small}}\langle 1|\,\mathbf{O}\,|L\rangle_{\text{large}}$ and $_{\text{small}}\langle L|\,\mathbf{O}\,|1\rangle_{\text{large}}$, with $L > 1$.

In general, the coupling constant $_{\text{small}}\langle L_2|\,\mathbf{O}\,|L_1\rangle_{\text{large}}$ can be evaluated as[31,32]

$$_{\text{small}}\langle L_2|\,\mathbf{O}\,|L_1\rangle_{\text{large}}$$
$$= -\frac{j\omega}{4}\int_{\text{small sphere}} dv(\epsilon_{\text{small}} - \epsilon_0)\mathbf{e}_{\mathbf{L_1}}^{\text{large}} \cdot \mathbf{e}_{\mathbf{L_2}}^{\text{small}*}, \quad (5)$$

where ϵ_{small} is the dielectric function of the small sphere, ϵ_0 is the vacuum permittivity, $\mathbf{e}_{\mathbf{L_1}}^{\text{large}}$ is the normalized electric field for the mode $|L_1\rangle_{\text{large}}$, and $\mathbf{e}_{\mathbf{L_2}}^{\text{small}}$ is the normalized electric field for the mode $|L_2\rangle_{\text{small}}$. The formula is derived by considering the energy transfer to the small sphere, due to the polarization field created by $|L_1\rangle_{\text{large}}$ in the small sphere region. Here, the integration occurs only inside the small sphere.

From Figs. 3(a) and 3(b), we see that the mode of the large sphere has a length scale of field variation that is much larger than the size of the small sphere. Therefore the field of the large sphere mode is nearly uniform within the small sphere, regardless of the order of the mode. In contrast, the mode of the small sphere can vary significantly inside the small sphere depending on L. The mode $|1\rangle_{\text{small}}$ has a uniform field distribution inside the small sphere. Therefore $_{\text{small}}\langle 1|\,\mathbf{O}\,|2\rangle_{\text{large}}$ is large, as can be seen in Fig. 3(a). In contrast, the mode $|2\rangle_{\text{small}}$ has a nodal plane inside the small sphere, and consequently, $_{\text{small}}\langle 2|\,\mathbf{O}\,|1\rangle_{\text{large}}$ is much smaller in magnitude [see Fig. 3(b)]. We show the magnitude of the coupling constant between the four lowest order modes for the two spheres in Fig. 3(c). Indeed, we see $|_{\text{small}}\langle 1|\,\mathbf{O}\,|L\rangle_{\text{large}}| \gg |_{\text{small}}\langle L|\,\mathbf{O}\,|1\rangle_{\text{large}}|$, for all $L > 1$.

The very large difference in $|_{\text{small}}\langle 1|\,\mathbf{O}\,|L\rangle_{\text{large}}|$ and $|_{\text{small}}\langle L|\,\mathbf{O}\,|1\rangle_{\text{large}}|$ with $L > 1$ should lead to large rectification. In the forward bias scenario, where the large sphere is maintained at temperature T_h and the small sphere is maintained at temperature T_l, there is an overlap of resonance frequencies between $|1\rangle_{\text{small}}$ and $|L\rangle_{\text{large}}$ with $L > 1$. Due to the large coupling constant $|_{\text{small}}\langle 1|\,\mathbf{O}\,|L\rangle_{\text{large}}|$ with $L > 1$, the net heat transfer should be large. In the reverse bias scenario, where the large sphere is maintained at temperature T_l and the small sphere is maintained at temperature T_h, there also is an overlap of resonance frequencies between $|1\rangle_{\text{large}}$ and $|L\rangle_{\text{small}}$, with $L > 1$. However, due to the significantly smaller coupling constant $|_{\text{small}}\langle L|\,\mathbf{O}\,|1\rangle_{\text{large}}|$ with $L > 1$, the net heat transfer should be greatly suppressed.

C. Numerical demonstration of rectification in two-sphere system

We verify the existence of large thermal rectification in the two-sphere system, by directly calculating the net heat transfer between two $3C$-SiC spheres using the partial-wave scattering method.[30] We present in Fig. 4(a) the net heat transfer magnitude for a different large sphere temperature T_1 and a small sphere temperature T_2. The diagonal line of Fig. 4(a) corresponds to the case where two bodies have equal temperatures, and hence the net heat transfer is zero, agreeing with the second law of thermodynamics. The strong asymmetry of Fig. 4(a) with respect to the diagonal line indicates strong rectification.

In Fig. 4(b), we plot the contrast ratio for a given set of temperature bias as specified by T_h and T_l, with $T_h \geqslant T_l$.
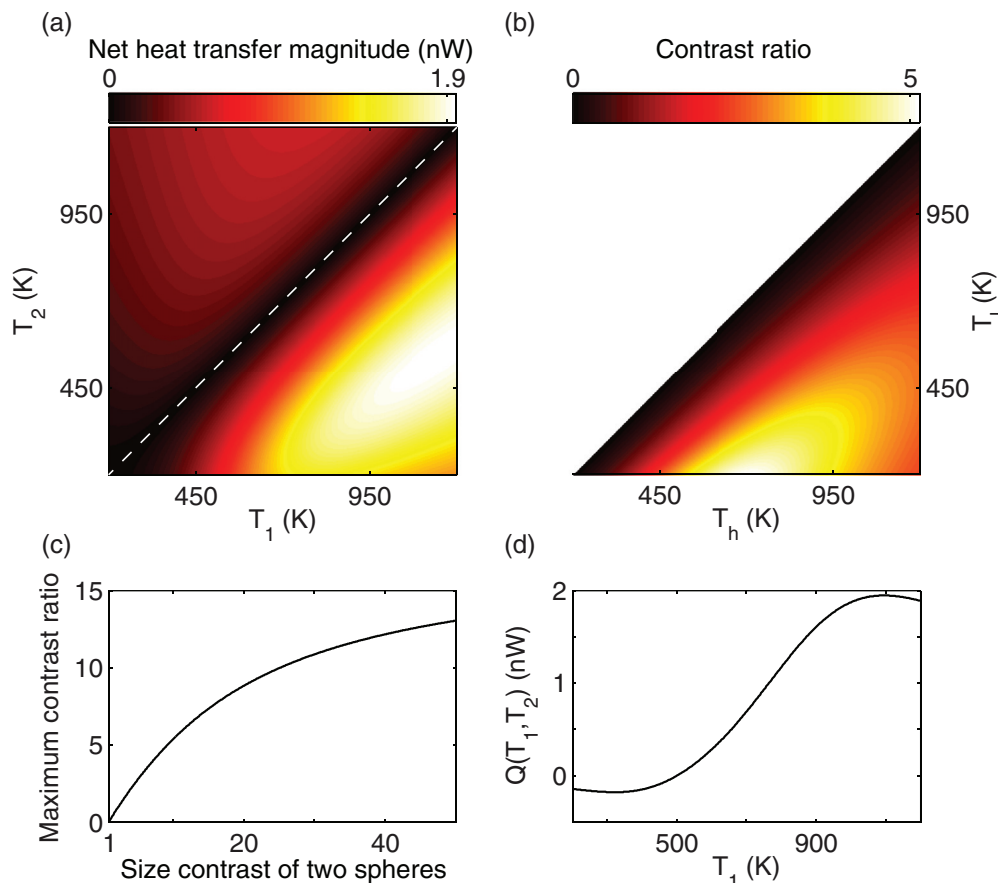
FIG. 4. (Color online) (a) Net heat transfer magnitude as a function of the larger sphere temperature T_1 and the small sphere temperature T_2. (b) Rectification contrast ratio for different sets of T_h and T_l. (a) and (b) use the same parameters of the representative device implementation [see Fig. 1(e)]. (c) Maximum rectification contrast ratio as a function of the contrast between the radii of the spheres (r_{large}/r_{small}), as the sphere-sphere distance is varied, for a temperature bias $T_h = 700$ K and $T_l = 200$ K. The small sphere has a radius of 10 nm. (d) The net heat transfer between two spheres as a function of the large sphere temperature T_1, where the small sphere is maintained at $T_2 = 500$ K, using the same parameters of the representative device implementation [see Fig. 1(e)].

The forward (reverse) bias scenario corresponds to the large (small) sphere having the higher temperature. The contrast ratio reaches a maximum of 5.14, when $T_h \approx 700$ K and $T_l \approx 200$ K.

In Fig. 4(c), we plot the maximum rectification contrast ratio as a function of the contrast between the radii of the spheres, for a temperature bias of $T_h = 700$ K and $T_l = 200$ K. The small sphere has a radius of 10 nm. We vary the radius of the large sphere. Each data point in Fig. 4(c) corresponds to the maximum rectification contrast ratio for a given radius of the large sphere, as the sphere-sphere distance is varied. We see that the maximum rectification ratio increases as the size difference between the spheres increases. This is expected from the modal analysis above. The contrast ratio here is at least an order of magnitude larger than the previous photon-based thermal rectification for similar material systems.[9–11] Since the modes of the spheres are scale invariant, the contrast in the length scale of the spatial variation of the modes become more prominent as the contrast in the sizes of the two spheres increases. In general, we found that in the deep-subwavelength regime, the contrast ratio is scale-invariant, i.e., the contrast ratio remains the same if we scale all the parameters of the device proportionally. We also emphasize that when the two

spheres are not in deep-subwavelength regime, even if there is large size contrast for the two spheres, the thermal rectification contrast ratio is negligible, and therefore the device is based on the unique properties of deep-subwavelength modes.

As a side note, we also observe negative differential thermal conductance in our device.[6,33] As an example, in Fig. 4(d), we plot the net heat transfer between the two spheres as a function of the large sphere temperature T_1, where the small sphere is maintained at a temperature $T_2 = 500$ K. The net heat transfer varies with T_1 nonmonotonously, exhibiting negative slopes at low- and high-temperature ends of the temperature range we consider here. In this system, as discussed earlier, the net heat flow is dominated by net heat transfer to the $L = 1$ mode $|1\rangle_{small}$ of the small sphere. In the regime where $T_1 < T_2$, the resonances of the larger sphere eventually become off-resonance with $|1\rangle_{small}$ as T_1 decreases [see Fig. 2(a)], resulting in the decrease of the magnitude of heat flow. On the other hand, in the regime where $T_1 > T_2$, there are always higher modes of the larger sphere that are on resonance with $|1\rangle_{small}$ [see Fig. 2(a)]. However, as T_1 increases, the modes in the large sphere that are on resonance have an increasing L [see Fig. 2(a)], resulting in the decrease of the coupling between the two spheres and hence a reduced net heat flow.
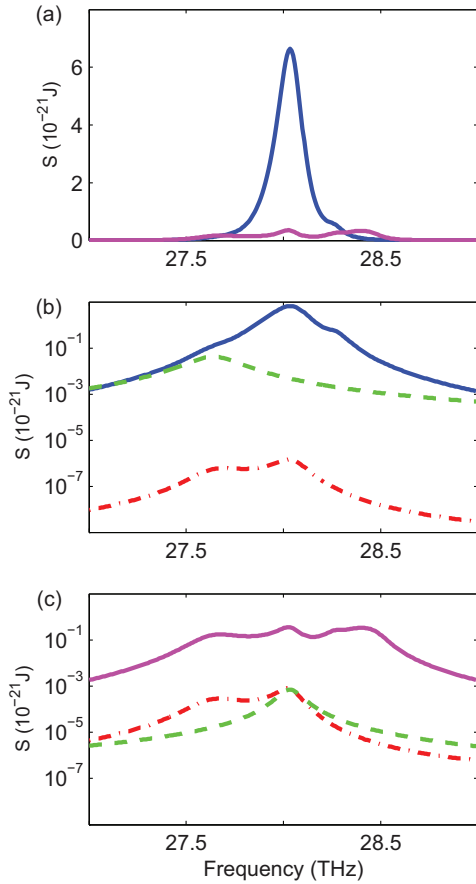
FIG. 5. (Color online) (a) Net heat transfer spectra in forward bias scenario (blue line), and reverse bias scenario (magenta line), for a bias condition $T_h = 700$ K, $T_l = 200$ K. (b) The net heat transfer spectrum (blue line), far-field radiation spectra of the large sphere (green dashed line) and the small sphere (red dash-dotted line) in the forward bias scenarios. (c) The net heat transfer spectrum (magenta line), far-field radiation spectra of the large sphere (green dashed line) and the small sphere (red dash-dotted line) in the reverse bias scenarios. (a)–(c) use the same parameters of the representative device implementation [see Fig. 1(e)].

In Fig. 5(a), we plot the spectra of the thermal transfer between the two spheres, for the bias condition of $T_h = 700$ K and $T_l = 200$ K. Under both the forward and the reverse bias scenarios [see Fig. 5(a)], the thermal transfer spectra are dominated by peaks near 28.03 THz, but the transfer strength in the reverse bias scenario is far weaker. These spectra are consistent with our theoretical analysis presented above; the spheres are indeed on resonance in both forward and reverse bias scenarios, but the coupling strength in the reverse bias scenarios are far weaker. Also, we see that the transfer spectra, in both forward and reverse bias scenario are dominated by the resonant components, as we can see by the solid lines in Figs. 5(b) and 5(c) where the spectra are presented on the logarithmic scale. The dominance of the spectral component of thermal transfer, even in the reverse bias case, is directly related to the high rectification contrast ratio we observe in the simulations.

In Figs. 5(b) and 5(c), we also compare the net heat transfer to the far-field thermal radiation from both spheres. The

net heat transfer completely dominates the far-field thermal radiation from the individual spheres, which indicates that as far as electromagnetic heat transfer is concerned, the rectifier here is very well isolated from the environment, and will have little interference with other electromagnetic thermal transfer devices.

D. Dynamic study

In a phonon-based thermal rectifier, the low speed of phonon propagation, which is typically in the magnitude of 1000 m/s, constrains the speed or the operating bandwidth.[34] A photon-based rectifier is not constrained by the speed of the heat carrier. Thus our device is expected to work in higher bandwidth than phonon-based thermal rectification. We now perform a dynamic study for the our thermal rectifier, and show that it can work in a bandwidth as high as 100 MHz.

To do the dynamic study, we introduce two thermal contacts with temperature τ_1 and τ_2. The two contacts are connected with the large and the small spheres, with thermal conductance of h_1 and h_2, respectively. We denote the net heat transfer between the spheres as $Q(T_1, T_2)$. The photon propagation between the spheres can be treated as instantaneous for such a nanoscale separation. The dynamical equations for T_1 and T_2 are therefore

$$C_1 \frac{dT_1}{dt} = h_1(\tau_1 - T_1) - Q(T_1, T_2), \quad (6)$$

$$C_2 \frac{dT_2}{dt} = h_2(\tau_2 - T_2) + Q(T_1, T_2), \quad (7)$$

where C_1 and C_2 are thermal capacitances for the large and the small spheres, respectively. In Eqs. (6) and (7), the relevant time scales are set by C_1/h_1 and C_2/h_2. A higher operation speed is obtained for small thermal capacitance C and large contact conductance h. Since the thermal capacitances are small for the spheres, with reasonable contact conductance we should expect to see a large operation bandwidth for these devices.

Recently, near-field heat transfer in sphere-plane geometry has been measured experimentally, where the thermal contact to the sphere is provided using a cantilever.[35–37] The contact conductance is 7910 nW/K in Ref. 36 and 4520 nW/K in Ref. 35 Therefore, in our dynamic study, we choose $h_1 = 4512$ nW/K, to be consistent with these experiments. We choose a smaller $h_2 = 5.1$ nW/K so that the intrinsic time constants of the spheres are comparable.

Our simulations assume a uniform temperature distribution within both spheres. The validity of this assumption requires the Biot number[38]

$$Bi \equiv \frac{H L_c}{\kappa} < 0.1. \quad (8)$$

Here, H is the heat transfer coefficient in units of W/m^2/K, L_c is the characteristic length scale, and κ is the thermal conductivity of the body. The Biot number Bi can be interpreted as the ratio of the heat transfer resistances inside and at the surface of a body. 3C-SiC has a typical thermal conductivity[39] of $\kappa = 360$ W/m/K. For a sphere, $H \approx h/(\pi r^2)$, $L_c \approx r$, and $Bi = h/(\pi r \kappa)$. For the large sphere, $h_1 = 4512$ nW/K, $r_1 = 96$ nm, and $Bi = 0.042$. For the small sphere, $h_2 = 5.1$ nW/K, $r_2 = 10$ nm, and $Bi = 0.00045$. Therefore both
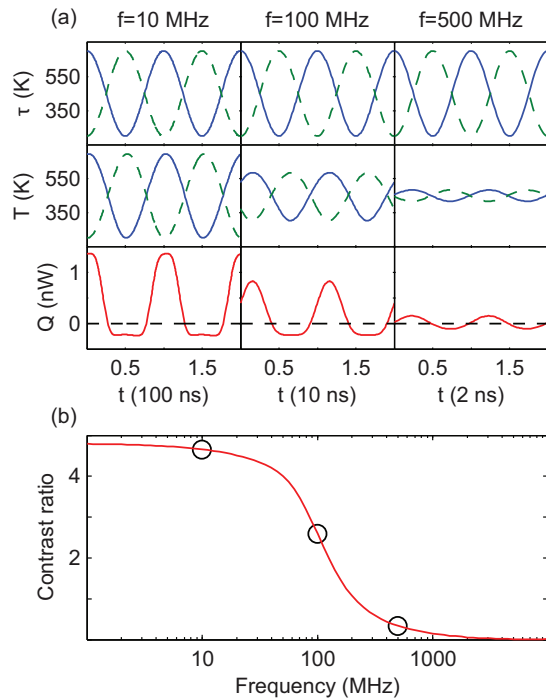
FIG. 6. (Color online) (a) Wave forms for the temperatures of the contacts τ_1 and τ_2, the temperatures of two spheres T_1 and T_2, and net heat transfer, in three frequencies, i.e., 10, 100, and 500 MHz, as denoted by the circles in (b). The first row shows wave forms of the temperatures of the contacts τ_1 (blue line) and τ_2 (green dashed line). The second row shows wave forms of the temperatures of the two spheres T_1 (blue line) and T_2 (green dashed line). The third row shows wave forms of net heat transfer $Q(T_1, T_2)$ (red line). The contact conductances are $h_1 = 4512$ nW, $h_2 = 5.1$ nW. (b) Frequency dependence of rectification contrast ratio for $A = 250$ K. (a) and (b) use the same parameters of the representative device implementation [see Fig. 1(e)].

spheres satisfy $Bi < 0.1$. Hence the assumption of a uniform temperature distribution within both spheres is reasonable. We note that for a specific sphere size the requirement for a uniform temperature distribution within both spheres puts an upper bound for the contact thermal conductances, which in turn leads to an upper bound for the operating bandwidth of our device.

We vary the temperature of the contact τ_1 and τ_2 sinusoidally:

$$\tau_1 = \tau_{10} + A\cos(2\pi ft), \tag{9}$$

$$\tau_2 = \tau_{20} - A\cos(2\pi ft), \tag{10}$$

where $\tau_{10} = \tau_{20} = 450$ K are the average temperatures for the two contacts and $A = 250$ K is amplitude of temperature fluctuations.

In Fig. 6(a), we show the wave forms of contact temperatures τ_1 and τ_2 (first row), temperatures for two bodies T_1 and T_2 (second row), and corresponding net heat transfer $Q(T_1, T_2)$ (third row), for three cases with different frequencies f, as denoted by circles in Fig. 6(b). For $f = 10$ MHz, T_1 and T_2 are almost the same as τ_1 and τ_2, and there is large rectification. For $f = 100$ MHz, there is a considerable phase lag between the temperature fluctuations of the spheres and contacts, and the rectification reduces. For the case of $f = 500$ MHz, there is very little temperature fluctuation on the spheres, the rectification almost completely vanishes. We define the operating bandwidth of the rectifier as the frequency at which the contrast ratio is reduced by 3 dB from that at $f = 0$ Hz. Examining Fig. 6(b), which plots the contrast ratio as a function of f, we see that the device has a bandwidth over 100 MHz.

IV. FINAL REMARKS AND CONCLUSIONS

We note that a spherical $3C$-SiC nanoparticle can be fabricated using various methods, including electrochemical etching,[40] chemical vapor synthesis,[41] and carbothermal reduction.[42] The heat flow in our device is on the order of nanowatt. Recent experiments have provided measurement resolution for heat flow at picowatt[43] and even subpicowatt[44] level. Therefore our proposed device for thermal rectification between nanoparticles should be within the regime where experiments may be conducted.

In conclusion, we have shown that near-field thermal transfer in the two-sphere geometry can provide a strong thermal rectification effect with ultrahigh contrast and large bandwidth, as well as negative differential thermal conductance. The underlying operating mechanism for achieving thermal rectification is fundamentally different from previous studies. Our work shows that the unique modal properties of nanophotonic structures can be exploited to create a powerful mechanism for achieving new thermal functionalities.

*shanhui@stanford.edu

[1]B. Li, L. Wang, and G. Casati, Phys. Rev. Lett. **93**, 184301 (2004).

[2]C. W. Chang, D. Okawa, A. Majumdar, and A. Zettl, Science **314**, 1121 (2006).

[3]G. Wu and B. Li, Phys. Rev. B **76**, 085424 (2007).

[4]W. Kobayashi, Y. Teraoka, and I. Terasaki, Appl. Phys. Lett. **95**, 171905 (2009).

[5]J. Hu, X. Ruan, and Y. P. Chen, Nano Lett. **9**, 2730 (2009).

[6]B. Li, L. Wang, and G. Casati, Appl. Phys. Lett. **88**, 143501 (2006).

[7]L. Wang and B. Li, Phys. Rev. Lett. **101**, 267203 (2008).

[8]R. Xie, C. T. Bui, B. Varghese, Q. Zhang, C. H. Sow, B. Li, and J. T. L. Thong, Adv. Funct. Mater. **21**, 1602 (2011).

[9]C. R. Otey, W. T. Lau, and S. Fan, Phys. Rev. Lett. **104**, 154301 (2010).

[10]S. Basu and M. Francoeur, Appl. Phys. Lett. **98**, 113106 (2011).

[11]H. Iizuka and S. Fan, J. Appl. Phys. **112**, 024304 (2012).

[12]L. P. Wang and Z. M. Zhang, Nanosc. Microsc. Therm. **17**, 337 (2013).

[13]K. Park and Z. M. Zhang, Front. Heat Mass Transfer **4**, 013001 (2013).

[14]B. Guha, C. R. Otey, C. B. Poitras, S. Fan, and M. Lipson, Nano Lett. **12**, 4546 (2012).

[15]P. J. van Zwol, K. Joulain, P. Ben Abdallah, J.-J. Greffet, and J. Chevrier, Phys. Rev. B **83**, 201404 (2011).

[16]P. J. van Zwol, L. Ranno, and J. Chevrier, Phys. Rev. Lett. **108**, 234301 (2012).

[17]P. J. van Zwol, K. Joulain, P. Ben-Abdallah, and J. Chevrier, Phys. Rev. B **84**, 161413 (2011).

[18]V. B. Svetovoy, P. J. van Zwol, and J. Chevrier, Phys. Rev. B **85**, 155418 (2012).

[19]O. Ilic, M. Jablan, J. D. Joannopoulos, I. Celanovic, H. Buljan, and M. Soljačić, Phys. Rev. B **85**, 155422 (2012).

[20]S.-A. Biehs, F. S. S. Rosa, and P. Ben-Abdallah, Appl. Phys. Lett. **98**, 243102 (2011).

[21]L. Cui, Y. Huang, J. Wang, and K.-Y. Zhu, Appl. Phys. Lett. **102**, 053106 (2013).

[22]C. F. Bohren and D. R. Huffman, *Absorption and Scattering of Light by Small Particles* (Wiley, New York, 1983), Chaps. 4, 5, and 12.

[23]W. G. Spitzer, D. A. Kleinman, and C. J. Frosch, Phys. Rev. **113**, 133 (1959).

[24]D. Olego and M. Cardona, Phys. Rev. B **25**, 3889 (1982).

[25]M. Wieligor, Y. Wang, and T. W. Zerda, J. Phys.: Condens. Matter **17**, 2387 (2005).

[26]G. Xi, S. Yu, R. Zhang, M. Zhang, D. Ma, and Y. Qian, J. Phys. Chem. B **109**, 13200 (2005).

[27]R. J. Nemanich, S. A. Solin, and R. M. Martin, Phys. Rev. B **23**, 6348 (1981).

[28]H. Richter, Z. Wang, and L. Ley, Solid State Commun. **39**, 625 (1981).

[29]C. F. Bohren and D. R. Huffman, *Absorption and Scattering of Light by Small Particles* (Wiley, New York, 1983), pp. 280–281.

[30]A. Narayanaswamy and G. Chen, Phys. Rev. B **77**, 075125 (2008).

[31]H. Haus, *Waves and Fields in Optoelectronics* (Prentice-Hall, NJ, 1984), pp. 226–228.

[32]H. Haus and W. Huang, J. Lightwave Technol. **5**, 16 (1987).

[33]L. Zhu, C. R. Otey, and S. Fan, Appl. Phys. Lett. **100**, 044104 (2012).

[34]L. Wang and B. Li, Phys. World **21**, 27 (2008).

[35]A. Narayanaswamy, S. Shen, and G. Chen, Phys. Rev. B **78**, 115303 (2008).

[36]S. Shen, A. Narayanaswamy, and G. Chen, Nano Lett. **9**, 2909 (2009).

[37]E. Rousseau, A. Siria, G. Jourdan, S. Volz, F. Comin, J. Chevrier, and J.-J. Greffet, Nat. Photon. **3**, 514 (2009).

[38]T. Bergman, A. Lavine, F. Incropera, and D. DeWitt, *Fundamentals of Heat and Mass Transfer*, 7th ed. (Wiley, Hoboken, NJ, 2011), pp. 283–285.

[39]M. Levinshtein, S. Rumyantsev, and M. Shur, *Properties of Advanced Semiconductor Materials: GaN, AlN, InN, BN, SiC, SiGe* (Wiley, New York, 2001).

[40]J. Y. Fan, X. L. Wu, H. X. Li, H. W. Liu, G. G. Siu, and P. K. Chu, Appl. Phys. Lett. **88**, 041909 (2006).

[41]S. Klein, M. Winterer, and H. Hahn, Chem. Vap. Deposition **4**, 143 (1998).

[42]K. J. Kim, S. Lee, J. H. Lee, M.-H. Roh, K.-Y. Lim, and Y.-W. Kim, J. Am. Ceram. Soc. **92**, 424 (2009).

[43]S. Sadat, Y. J. Chua, W. Lee, Y. Ganjeh, K. Kurabayashi, E. Meyhofer, and P. Reddy, Appl. Phys. Lett. **99**, 043106 (2011).

[44]C. Canetta and A. Narayanaswamy, Appl. Phys. Lett. **102**, 103112 (2013).